Supporting Information

Modulation morphology and electronic structure of Ni_3S_2 nano-forest via P and Mo co-doped in polyoxometalate to promote urea oxidation reaction

Yao Zhang*[a], Haoran Guo*[b], Ming Song[a], Limei Sun[a], and Rui Song*[b]

[a] School of Materials and Chemical Engineering, Xuzhou University of Technology, Xuzhou 221018, PR China

[b] School of Chemical Sciences, University of Chinese Academy of Sciences, 19 Yuquan Road, Shijingshan District, Beijing, 100049, PR China

*Yao Zhang, Lecturer, Ph.D, Corresponding author, Email: zhangyao@xzit.edu.cn
*Haoran Guo, Ph.D candidate, Corresponding author, Email: guohran@163.com
*Rui Song, Professor, Ph.D, Corresponding author, Email: rsong@ucas.ac.cn

Experimental Section

Chemicals and Reagents

Phosphomolybdic acid ($PMo_{12}O_{40}\cdot xH_2O$), Ammonium molybdate tetrahydrate ($(NH_4)_6Mo_7O_{24}\cdot 4H_2O$), iridium dioxide ($IrO_2$) were purchased from Shanghai Macklin Biochemical Industrial Co., Ltd. Thiourea (CH_4N_2S) was purchased from Aladdin Industrial Co., Ltd. All chemicals were used as received without further purification. Ni foam (NF, thickness 0.5 mm) was purchased from Guangzhou Lige Technology Co., Ltd. Before useing, NF was ultrasonically cleaned in 6 M HCl solution for 15 min to remove the surface nickel oxide layer; then NF was ultrasoniced in acetone, ethanol and water for 30 min respectively. Finally, dry in a vacuum oven at 50 °C to avoid further oxidation. The deionized water (18.2 MΩ cm) was used throughout the whole experiments.

Electrode materials characterizations

Scanning electron microscopy (SEM) was carried out on a Hitachi SU8220. Transmission electron microscopy (TEM) and energy-dispersive X-ray spectroscopy (EDS) elemental mapping attached to the TEM was performed on a FEI Talos F200X TEM microscope operated at 200 KV. X-ray diffraction (XRD) were collected on a Rigaku Smartlab diffractometer with Cu Kα1 (λ = 1.5406 Å) source. Raman spectra were examined using a Renishaw Invia Raman spectrometer with a 532 nm laser source. X-ray photoelectron spectra (XPS) were measured by a Thermo Scientific ECSALab 250Xi X-ray photoelectron spectrometer with an Al Kα X-ray radiation (1486 eV). The inductively coupled plasma mass spectrometry (ICP-MS) was measured by a Agilent ICPMS7800.

Electrochemical Measurements

All the electrochemical measurements were conducted in a standard three-electrode setup on a CHI 660E electrochemical workstation (Chenhua Instruments, Shanghai, China). A H-cell with a glass frit separating the anodic and cathodic compartments was used (three-electrode configuration). The fabricated self-supported electrodes (1 × 0.5 cm) were directly employed as working electrodes, while a graphite rod and an Hg/HgO (filled in 1 M KOH) electrode as

the counter electrode and the reference electrode, respectively. For comparison, 5 mg of IrO_2 and 50 μL of 5 wt% Nafion solution were dispersed in 950 μL of isopropyl alcohol by sonication for 1 h. Then the homogeneous suspension was drop-cast onto treated NF electrode where the total effective loading surface area of noble-metal catalysts is 1 cm^2, and the mass loading is 1.5 mg cm^{-2}. Before Multiple cyclic voltammetry (CV) scans were firstly performed at a scan rate of 5 mV s^{-1} until reached a stable state of electrodes. Then, linear sweep voltammetry (LSV) was conducted with a scan rate of 2 mV s^{-1} in 1 M KOH with 0.5 M urea solution. The electrochemical impedance spectroscopy (EIS) measurements were carried out at a potential of 1.36 V vs. RHE for the UOR over a frequency range from 100 kHz to 0.01 Hz with an amplitude of 10 mV. The long-term stability was tested by chronopotentiometry and multiple cycles of CV scans. All the polarization curves were corrected using 90% *iR* compensation. Potentials were referenced to the reversible hydrogen electrode (RHE): *E* vs. RHE = *E* vs. Hg/HgO + 0.098 + 0.059 pH.

Calculation of ECSA

Based on the literature [1], cyclic voltammetry (CV) was carried out in 1 M KOH with 0.5 M urea solution to probe the electrochemical double-layer capacitance of the various samples at non-Faradic overpotentials to estimate the effective electrode surface areas. Accordingly, a series of CV measurements were performed at various scan rates (20, 40, 60, 80 and 100 mV s^{-1}) in 0.95 – 1.05 V vs. RHE range, and the sweep segments of the measurements were set to 10 to ensure consistency. By plotting the difference in current density (J) between the anodic and cathodic sweeps ($J_{anodic} - J_{cathodic}$) at 1 V vs. RHE against the scan rate, a linear trend was observed. The slope of the fitting line was found to be equal-to-twice the geometric double-layer capacitance (C_{dl}), which was proportional to the effective electrode surface area of the materials. Therefore, the electrochemical surface areas of different samples can be compared with one another based on their C_{dl} values. However, it should be noted that this comparison makes sense only when the measurement of materials was carried out under the same condition.

The electrochemically active surface area (ECSA) was calculated from the C_{dl} value following the equations:

$$ECSA = \frac{C_{dl}}{40\ \mu F\ cm^{-2}\ per\ cm^{2}_{ECSA}}$$

DFT calculation

Computational methods

First-principles calculations were performed within the density functional theory framework [2]. The projector-augmented wave (PAW) method [3, 4] and the generalized gradient approximation (GGA) [5] for the exchange-correlation energy functional, as implemented in the Vienna ab initio simulation package (VASP) [6-8] were used. The GGA calculation was performed with the Perdew-Burke-Ernzerhof (PBE) [9] exchange-correlation potential. Considered long-range interaction between molecules/intermediates and surface, Van der Waals interactions were considered using DFT-D3 correlation. To avoid effects come from other slabs, a vacuum of 20 Å was added along z direction. The convergence criterion of geometry relaxation was set to 0.01 eV·Å^{-1} in force on each atom. The energy cutoff for plane wave-basis was set to 500 eV. The K points were sampled with 3×3×1 by Monkhorst-Pack method.

Calculation of the adsorption energies of urea (E_{ads}(urea)) and the desorption energies of *COO (E_{des}(*COO))

The adsorption energies of urea (E_b(urea)) and the desorption energies of *COO (E_{des}(*COO)) are calculated by the following equation [10]:

$$E_{ads}(urea) = E_{*urea} - E_{surface} - E_{urea}$$

$$E_{des}(*COO) = E_{surface} + E_{CO_2} - E_{*COO}$$

where E_{*urea}, $E_{surface}$, E_{urea}, E_{CO_2} and E_{*COO} are the calculated energies of the urea adsorption configuration, clean catalyst surface, urea molecule, CO_2 molecule and the *COO adsorption intermediate, respectively.

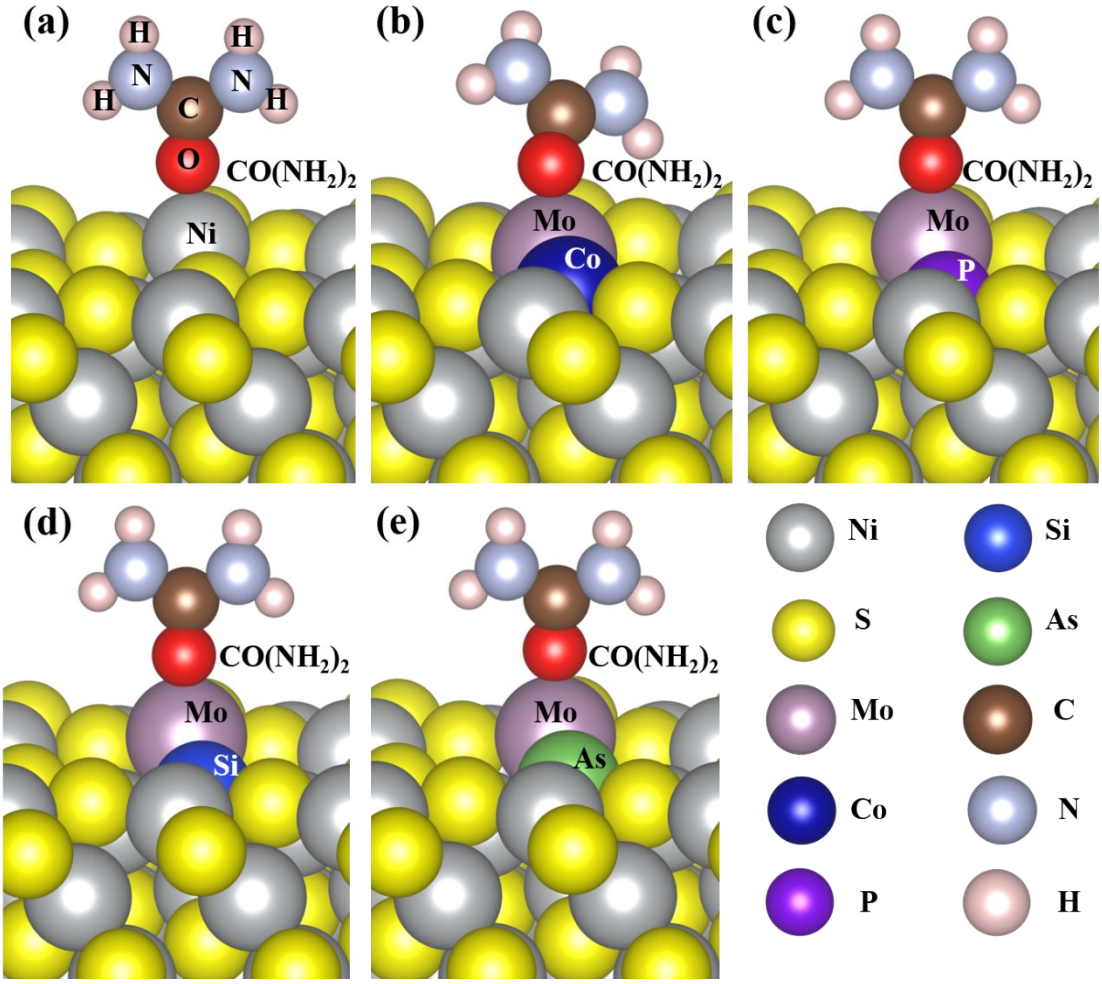

Fig. S1 The structural models of (**a**) Ni_3S_2, (**b**) Co-Mo-Ni_3S_2, (**c**) P-Mo-Ni_3S_2, (**d**) Si-Mo-Ni_3S_2, and (**e**) As-Mo-Ni_3S_2, for urea adsorption.

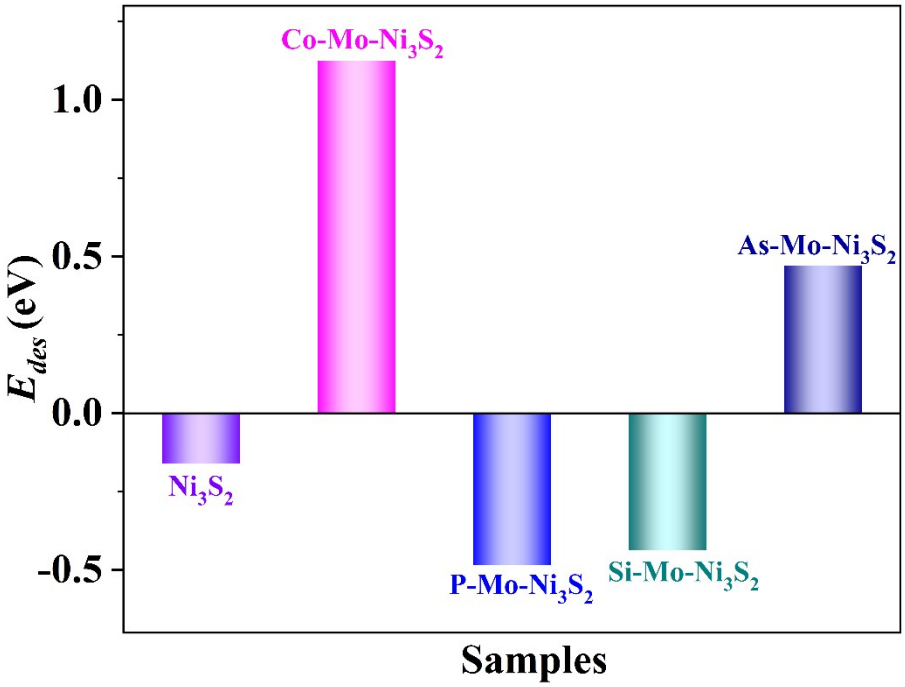

Fig. S2 The desorption of *COO intermediate on the pristine Ni_3S_2 and X-Mo-Ni_3S_2 (X=Co, P, Si, As) surfaces.

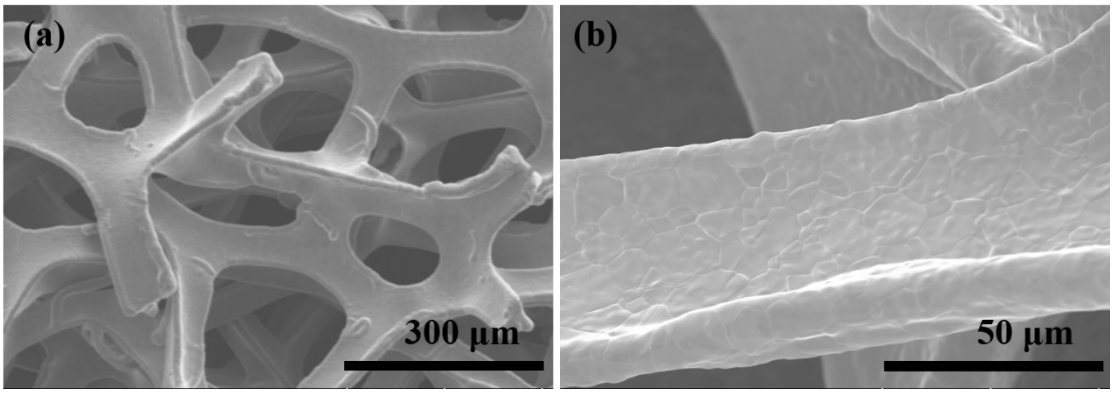

Fig. S3 (**a**, **b**) SEM images of pristine NF at different magnifications.

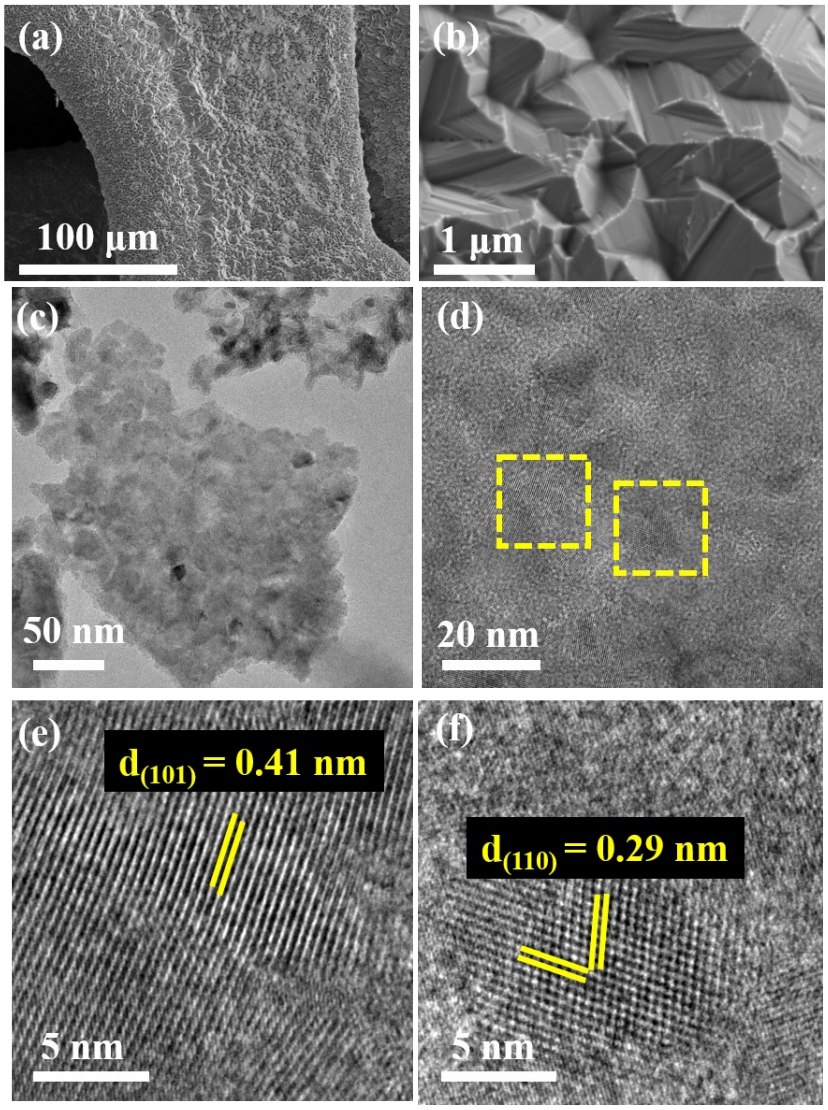

Fig. S4 (**a**, **b**) SEM images of Ni_3S_2@NF under different magnifications; (**c**) TEM image and (**d-f**) HRTEM images of Ni_3S_2@NF.

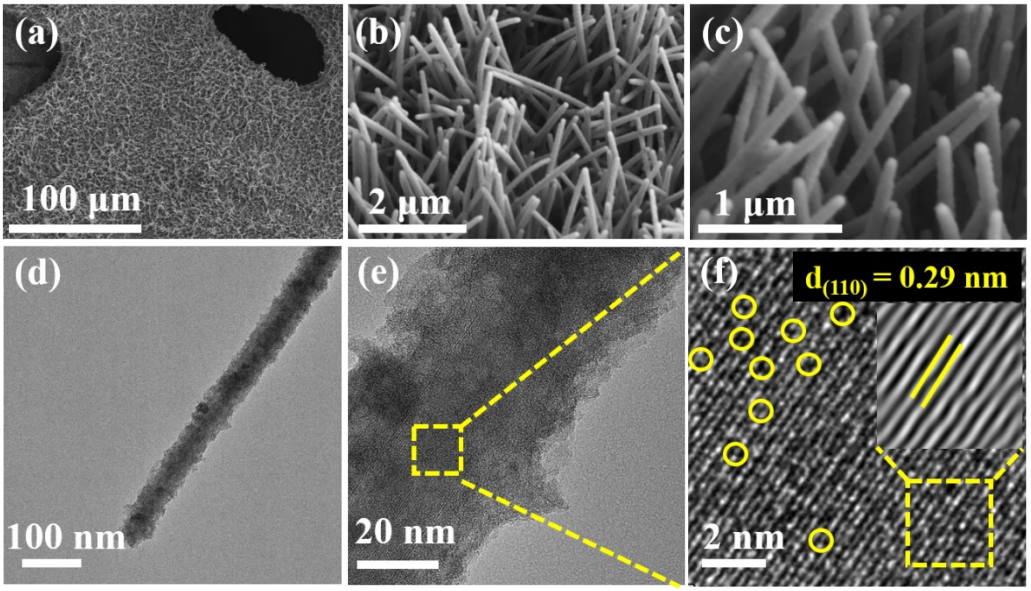

Fig. S5 (**a-c**) SEM images of Mo-Ni_3S_2@NF under different magnification; (**d**) TEM image and (**e**, **f**) HRTEM images of Mo-Ni_3S_2@NF.

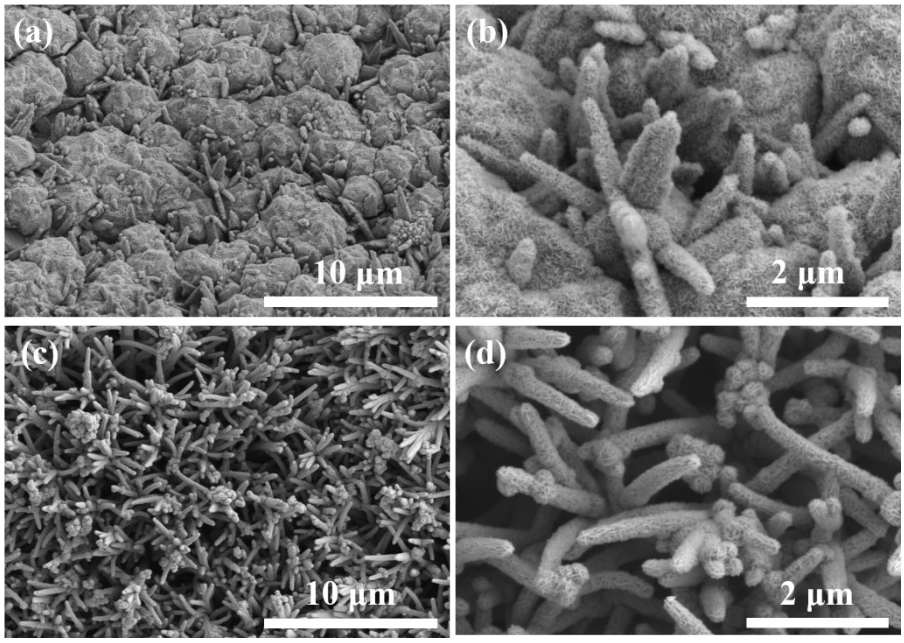

Fig. S6 (**a**, **b**) SEM images of 1:6 under different magnifications; (**c**, **d**) SEM images of 1:2 under different magnifications.

When PMo_{12} is not added to the precursor, the bare Ni_3S_2@NF electrode displays a bulky micrometer-sized (**Fig. S4**). The content of thiourea is fixed, and the effect of different P and Mo doping on the morphology of the catalyst is investigated by controlling the amount of PMo_{12} added (**Fig. 3** and **Fig. S6**). As shown in **Fig. S6a** and **S6b**, the SEM image of 1:6 still retains large micrometer-scale morphology, but many thin nanosheets appear on its surface. The morphology of the P-Mo-Ni_3S_2@NF electrode (S: Mo = 1:4) shows nano-forest superstructures with a thin layer of nanosheets covered on the surface of nano-trees (**Fig. 3**). When the doping amount of P and Mo continues to increase (S: Mo = 1:2), the nanoforest morphology remains, but the size of the nanosheets grown on the surface becomes larger (**Fig. S6c** and **S6d**).

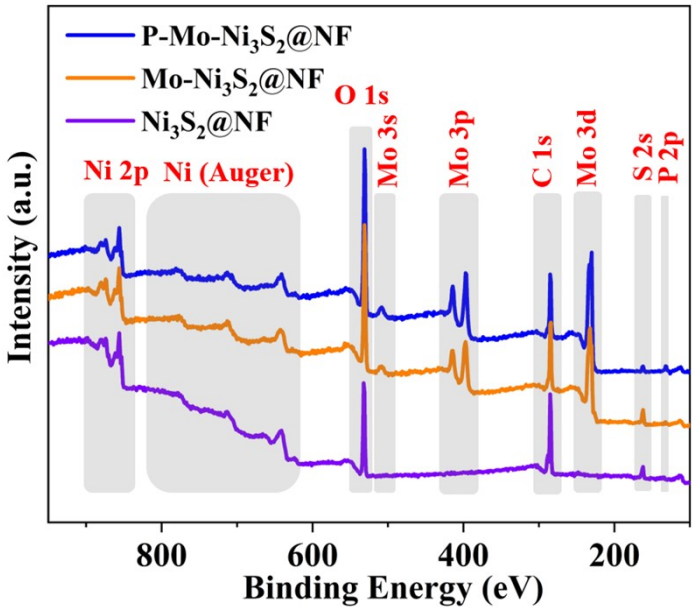

Fig. S7 XPS survey scan of P-Mo-Ni_3S_2@NF, Mo-Ni_3S_2@NF and Ni_3S_2@NF.

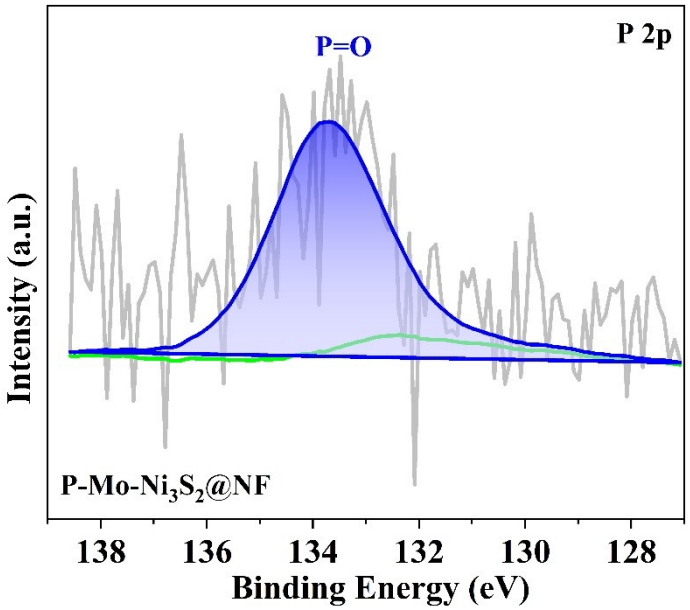

Fig. S8 XPS spectrum of P 2p in P-Mo-Ni_3S_2@NF.

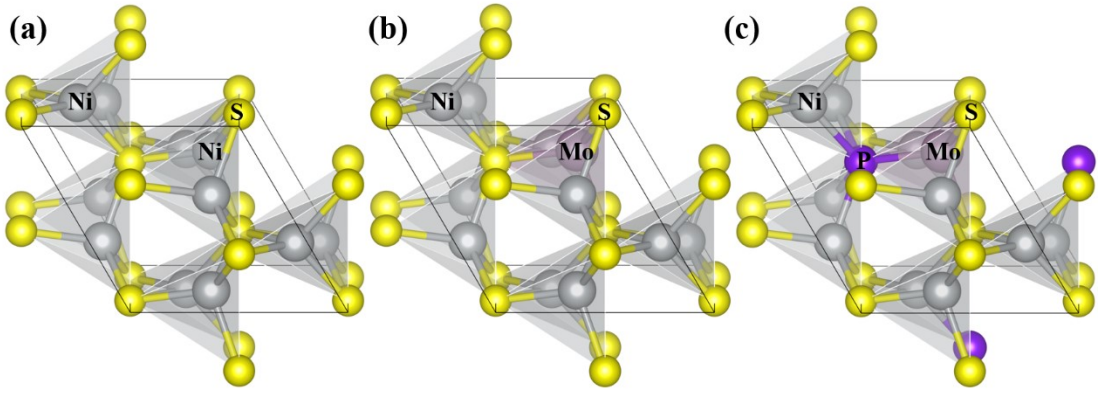

Fig. S9 The structural models of (**a**) Ni_3S_2, (**b**) Mo-Ni_3S_2 and (**c**) P-Mo-Ni_3S_2.

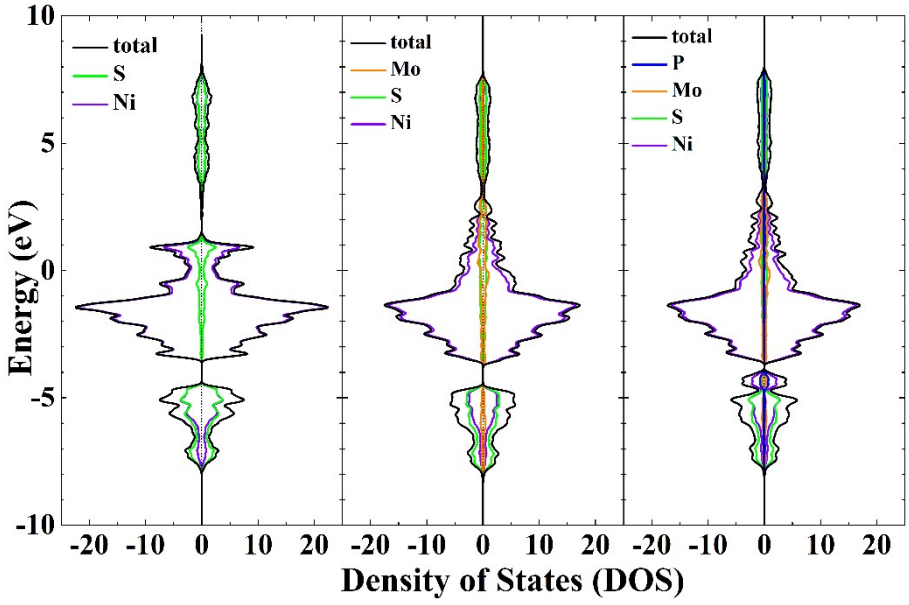

Fig. S10 The DOS calculation of Ni_3S_2, Mo-Ni_3S_2 and P-Mo-Ni_3S_2.

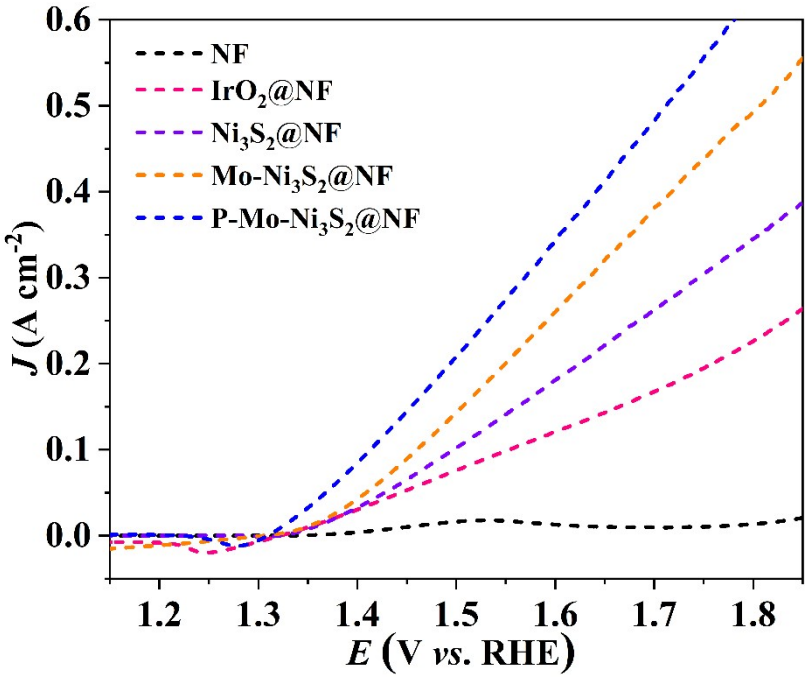

Fig. S11 LSV curves of NF, IrO_2@NF, Ni_3S_2@NF, Mo-Ni_3S_2@NF and P-Mo-Ni_3S_2@NF without compensation.

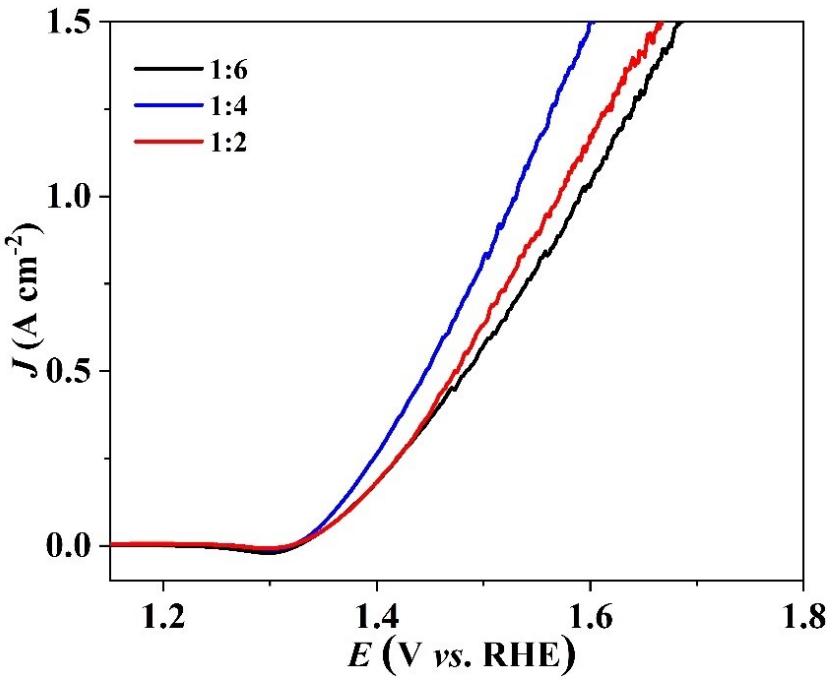

Fig. S12 Comparison of UOR activities of samples with thiourea precursor amount of 0.18 g synthesized at different mole ratios of Mo and S in 1 M KOH with 0.5 M urea.

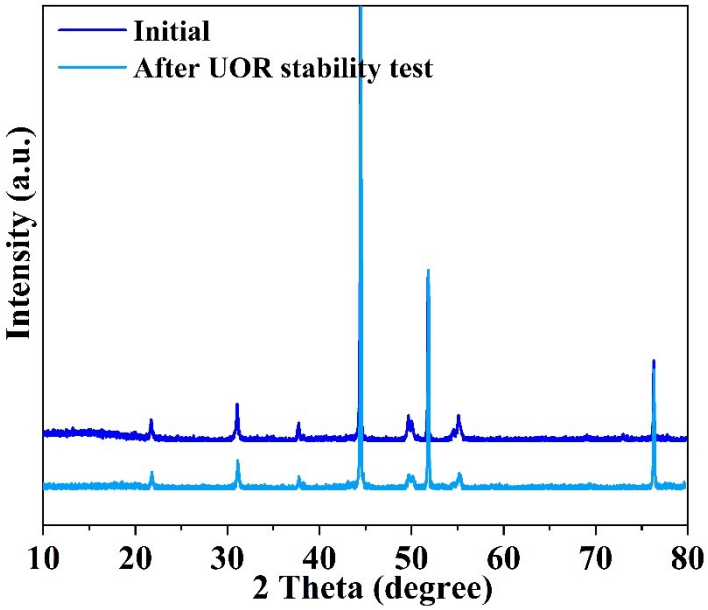

Fig. S13 XRD patterns of P-Mo-Ni_3S_2@NF after UOR stability test.

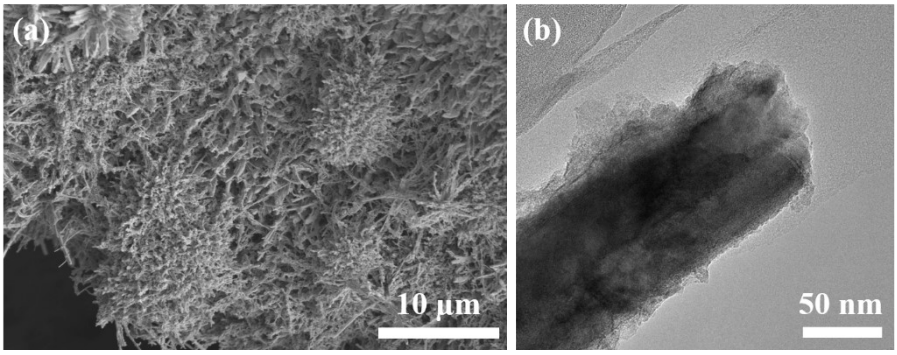

Fig. S14 (**a**) SEM image and (**b**) TEM image of the P-Mo-Ni_3S_2@NF electrode after UOR stability test.

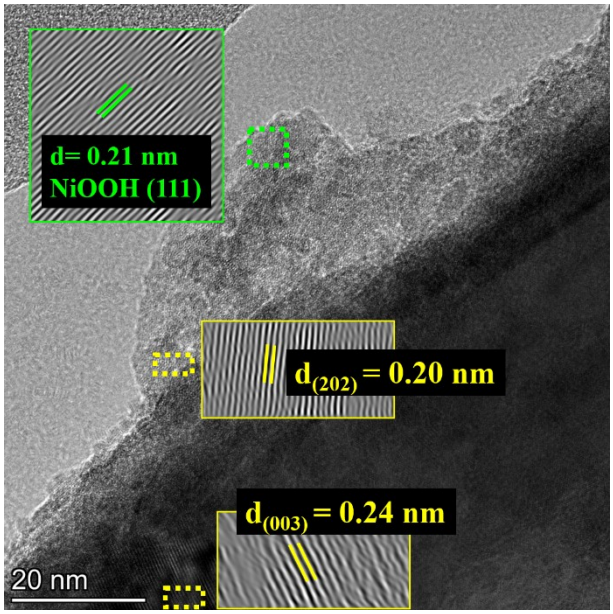

Fig. S15 HRTEM image of P-Mo-Ni_3S_2@NF after UOR stability test.

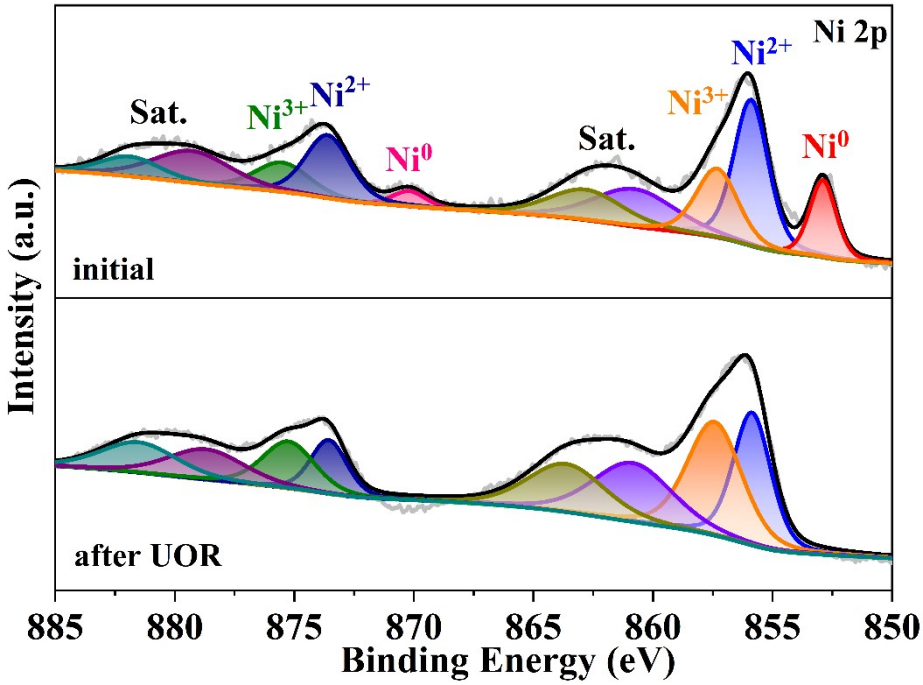

Fig. S16 Ni 2p XPS spectra of the P-Mo-Ni_3S_2@NF electrode before and after the UOR test.

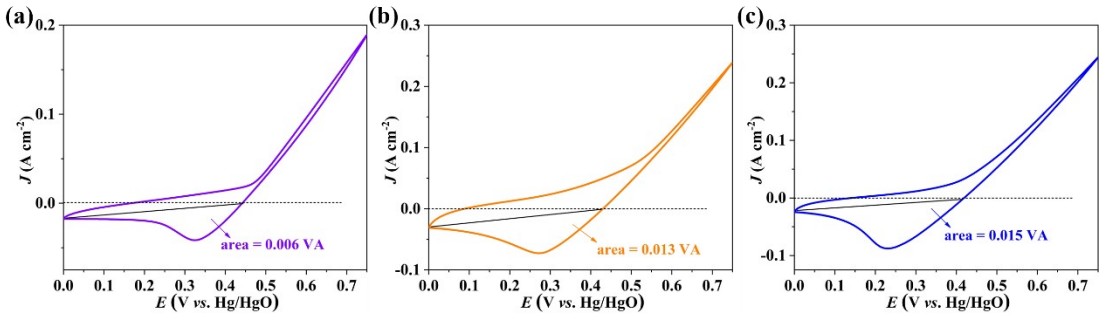

Fig. S17 Reduction peaks recorded at 0.1 V s^{-1} for determination of numbers of surface-active sites: (**a**) Ni_3S_2@NF, (**b**) Mo-Ni_3S_2@NF and (**c**) P-Mo-Ni_3S_2@NF.

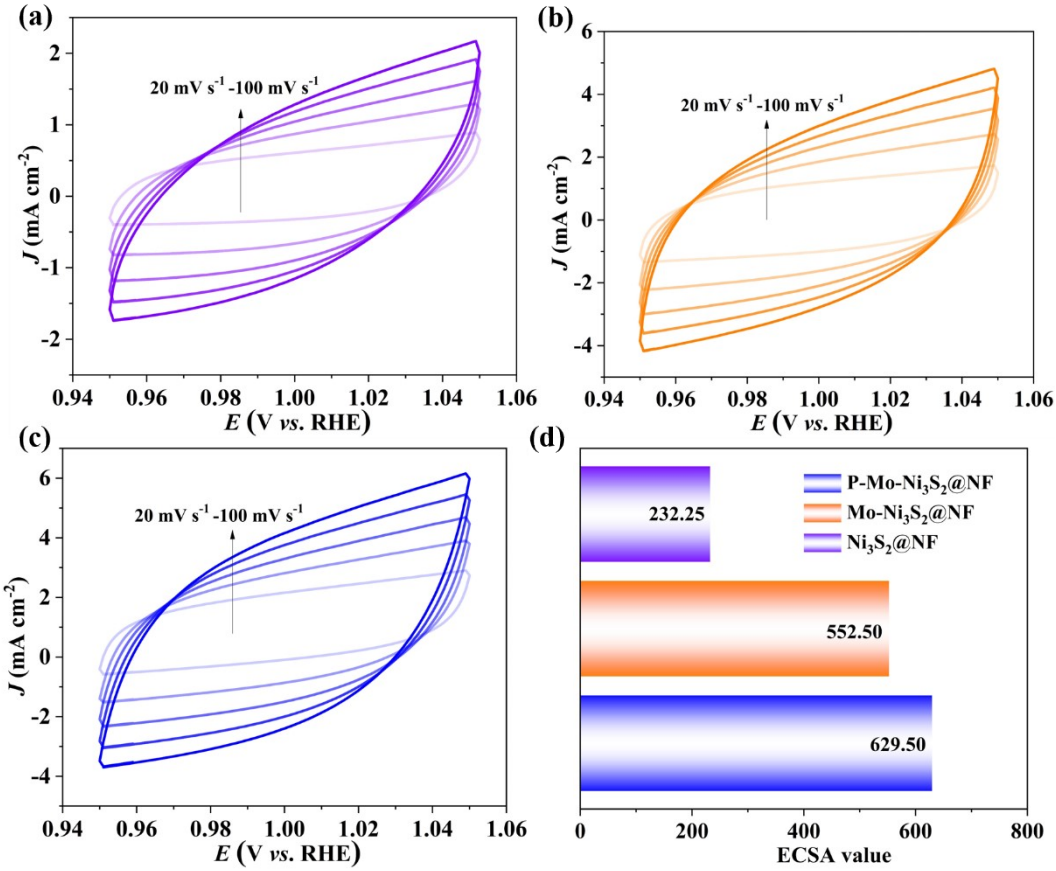

Fig. S18 CV curves of (**a**) Ni_3S_2@NF, (**b**) Mo-Ni_3S_2@NF and (**c**) P-Mo-Ni_3S_2@NF at varying scan rates (20−100 mV s^{-1}); (**d**) The ECSA values of Ni_3S_2@NF, Mo-Ni_3S_2@NF and P-Mo-Ni_3S_2@NF in 1 M KOH with 0.5 M urea for UOR.

Table S1 The content of Ni^0, Ni^{2+} and Ni^{3+} in the Ni_3S_2@NF, Mo-Ni_3S_2@NF and P-Mo-Ni_3S_2@NF electrodes

Content	Ni^0	Ni^{2+}	Ni^{3+}
Ni_3S_2@NF	16.04%	32.24%	17.39%
Mo-Ni_3S_2@NF	10.69%	32.90%	18.66%
P-Mo-Ni_3S_2@NF	9.55%	34.97%	21.16%
P-Mo-Ni_3S_2@NF-UOR	0	24.26%	30.19%

Table S2 Comparison of UOR performances for P-Mo-Ni_3S_2@NF with various reported electrocatalysts in the alkaline media with urea

electrocatalysts	electrolyte	Potential at 100 mA cm^{-2} (V)	Tafel slope ($mV\ dec^{-1}$)	Ref.
Mn-Ni_3S_2/NF	1.0 M KOH + 0.5 M Urea	1.40	41.7	[11]
NiS_2-MoS_2	1.0 M KOH + 0.33 M Urea	1.54	29.9	[12]
O-NiMoP/NF	1.0 M KOH + 0.5 M Urea	1.41	34	[13]
P-Mo-$Ni(OH)_2$	1.0 M KOH + 0.1 M Urea	1.39	/	[14]
P-$CoNi_2S_4$	1.0 M KOH + 0.5 M Urea	1.56	40	[15]
$Mo_{0.05}$, Co-NSH	1.0 M KOH + 0.5 M Urea	1.42	64.4	[16]
NiS@Ni_3S_2@ $NiMoO_4$	1.0 M KOH + 0.5 M Urea	1.45	30	[17]
Ni_3S_2-NiS/NF	1.0 M KOH + 0.5 M Urea	1.37	39	[18]
Ni_2P/Fe_2P/NF	1.0 M KOH + 0.5 M Urea	1.46	79.1	[19]
Fe-Ni_3S_2@$FeNi_3$-8	1.0 M KOH + 0.33 M Urea	1.45	29	[20]
Cu:α$Ni(OH)_2$/NF	1.0 M KOH + 0.33 M Urea	1.41	37.8	[21]
MoS_2/Ni_3S_2 /Ni/NF	1.0 M KOH + 0.33 M Urea	1.35	42	[22]
Mo-doped Ni_3S_2	1.0 M KOH + 0.3 M Urea	1.38	28	[23]
α/β-$NiMoO_4$@NF	1.0 M KOH + 0.5 M Urea	1.36	44.2	[24]
Ni_3S_2@NF	1.0 M KOH + 0.5 M Urea	1.42	58.4	This work
Mo-Ni_3S_2@NF	1.0 M KOH + 0.5 M Urea	1.38	79.2	This work
P-Mo-Ni_3S_2@NF	**1.0 M KOH + 0.5 M Urea**	**1.36**	**35.5**	**This work**

Table S3 The value of solution resistances (R_s) and charge transfer resistances (R_{ct})

Surface	R_s(Ω)	R_{ct} (Ω)
P-Mo-Ni_3S_2@NF	3.36	0.80
Mo-Ni_3S_2@NF	3.36	0.99
Mo-Ni_3S_2@NF	3.86	3.48
IrO_2@NF	3.54	3.00

References

1. J. F. Xie, S. Li, X. D. Zhang, J. J. Zhang, R. X. Wang, H. Zhang, B. C. Pan and Y. Xie, *Chem. Sci.*, 2014, **5**, 4615-4620.
2. W. Kohn and L. J. Sham, *Phys. Rev.*, 1965, **140**, A1133-1138.
3. P. E. Blöchl, *Phys. Rev. B*, 1994, **50**, 17953-17979.
4. G. Kresse and D. Joubert, *Phys. Rev. B*, 1999, **59**, 1758-1775.
5. J. P. Perdew and Y. Wang, *Phys. Rev. B*, 1992, **45**, 13244-13249.
6. G. Kresse and J. Hafner, *Phys. Rev. B*, 1993, **47**, 558-561.
7. G. Kresse and J. Furthmüller, *Phys. Rev. B*, 1996, **54**, 11169-11186.
8. G. Kresse and J. Furthmüller, *Comput. Mater. Sci.*, 1996, **6**, 15-50.
9. J. P. Perdew, K. Burke and M. Ernzerhof, *Phys. Rev. Lett.*, 1996, **77**, 3865-3868.
10. H. Guo, P. Yuan, J. Zhao, J. Zhao, Q. Peng and R. Song, *Chem. Eng. J.*, 2022, **450**, 138198. .
11. H. Yang, M. Yuan, Z. Sun, D. Wang, L. Lin, H. Li and G. Sun, *ACS Sustainable Chem. Eng.*, 2020, **8**, 8348-8355.
12. S. Wang, L. Zhao, J. Li, X. Tian, X. Wu and L. Feng, *J. Energy Chem.*, 2022, **66**, 483-492.
13. H. Jiang, M. Sun, S. Wu, B. Huang, C. S. Lee and W. Zhang, *Adv. Funct. Mater.*, 2021, **31**, 2104951.
14. W. Zhang, Y. Tang, L. Yu and X.-Y. Yu, *Appl. Catal. B-Environ.*, 2020, **260**, 118154.
15. X. F. Lu, S. L. Zhang, W. L. Sim, S. Gao and X. W. D. Lou, *Angew. Chem. Int. Ed.*, 2021, **60**, 22885-22891.
16. W. Huang, Y. Yuan, K. Wang, Q. Cao, Y. Zhao, X. Sun, R. Ding, P. Gao, W. Cai and E. Liu, *J. Electro. Chem.*, 2022, **911**, 116242.
17. L. Sha, T. Liu, K. Ye, K. Zhu, J. Yan, J. Yin, G. Wang and D. Cao, *J. Mater. Chem. A*, 2020, **8**, 18055-18063.
18. Q. Zhao, C. Meng, D. Kong, Y. Wang, H. Hu, X. Chen, Y. Han, X. Chen, Y. Zhou and M. Lin, *ACS Sustainable Chem. Eng.*, 2021, **9**, 15582-15590.
19. L. Yan, Y. Sun, E. Hu, J. Ning, Y. Zhong, Z. Zhang and Y. Hu, *J. Colloid Interface Sci.*, 2019, **541**, 279-286.
20. W. Zhang, Q. Jia, H. Liang, L. Cui, D. Wei and J. Liu, *Chem. Eng. J.*, 2020, **396**, 125315.
21. J. Xie, L. Gao, S. Cao, W. Liu, F. Lei, P. Hao, X. Xia and B. Tang, *J. Mater. Chem. A*, 2019, **7**, 13577-13584.
22. F. Li, J. Chen, D. Zhang, W. F. Fu, Y. Chen, Z. Wen and X. J. Lv, *Chem. Commun.*, 2018, **54**, 5181-5184.
23. H. Xu, Y. Liao, Z. Gao, Y. Qing, Y. Wu and L. Xia, *J. Mater. Chem. A*, 2021, **9**, 3418-3426.
24. Y. Zhang, H. Guo, X. Li, W. Ren and R. Song, *Mater. Chem. Front.*, 2022, **6**, 1477-1486.